Science Bulletin 64 (2019) 1584–1591

Contents lists available at ScienceDirect

Science Bulletin

journal homepage: www.elsevier.com/locate/scib

Article

# Electron-nuclear hyperfine coupling in quantum kagome antiferromagnets from first-principles calculation and a reflection of the defect effect

Shunhong Zhang[a], Yi Zhou[b,c,d], Feng Liu[e,f], Zheng Liu[a,f,*]

[a] Institute for Advanced Study, Tsinghua University, Beijing 100084, China
[b] Beijing National Laboratory for Condensed Matter Physics, and Institute of Physics, Chinese Academy of Sciences, Beijing 100190, China
[c] CAS Center for Excellence in Topological Quantum Computation, University of Chinese Academy of Sciences, Beijing 100190, China
[d] Collaborative Innovation Center of Advanced Microstructures, Nanjing 210093, China
[e] Department of Materials Science and Engineering, University of Utah, Salt Lake City, Utah 84112, USA
[f] Collaborative Innovation Center of Quantum Matter, Beijing 100084, China

ARTICLE INFO

*Article history:*
Received 15 June 2019
Received in revised form 31 July 2019
Accepted 16 August 2019
Available online 28 August 2019

*Keywords:*
Quantum spin liquid
Nuclear magnetic resonance
First-principles calculation
Defect effect

ABSTRACT

The discovery of ideal spin-1/2 kagome antiferromagnets Herbertsmithite and Zn-doped Barlowite represents a breakthrough in the quest for quantum spin liquids (QSLs), and nuclear magnetic resonance (NMR) spectroscopy plays a prominent role in revealing the quantum paramagnetism in these compounds. However, interpretation of NMR data that is often masked by defects can be controversial. Here, we show that the most significant interaction strength for NMR, i.e. the hyperfine coupling (HFC) strength, can be reasonably reproduced by first-principles calculations for these proposed QSLs. Applying this method to a supercell containing Cu-Zn defects enables us to map out the variation and distribution of HFC at different nuclear sites. This predictive power is expected to bridge the missing link in the analysis of the low-temperature NMR data.

## 1. Introduction

Quantum spin liquid (QSL) [1–3] is an emergent quantum phase in solid states that activates several fields of frontier physics, such as quantum magnetism, topological order [4], and high-temperature superconductivity [5,6]. For decades, kagome antiferromagnets have been intensively searched and studied as candidates to realize the QSL state [7,8]. Significant advances have been made, with synthetic Herbertsmithite ($Cu_3Zn(OH)_6Cl_2$, Fig. 1a) as a prototypical example [9–11]. Recently, first-principles calculations suggested Zn-doped Barlowite ($Cu_3Zn(OH)_6FBr$, Fig. 1b) as a sibling QSL candidate [12] and subsequent experiments observed promising signals [13,14]. The two compounds share a similar layered kagome spin lattice formed by $S = 1/2$ $Cu^{2+}$ ions. The absence of long-range magnetic order in these kagome magnets, a feature of QSL, preserves down to several tens of mK, despite the fact that the primary nearest neighbor (NN) antiferromagnetic (AFM) interaction is of the order of $10^2$ K [9,13,14].

Experimentally, one severe obstacle to clarifying the nature of the QSL ground state is the defect spin dynamics [15]. For example, macroscopic susceptibility measurements on both Herbertsmithite [9] and Zn-Barlowite [13] revealed Curie-like divergence at the low temperature overwhelming the intrinsic kagome AFM susceptibility, which is perceived as a consequence of isolated spins from extra $Cu^{2+}$ ions between the kagome layers.

Nuclear magnetic resonance (NMR) spectroscopy has played a prominent role in detecting the magnetic order in solids. By detecting the nuclear resonance peaks in presence of an external magnetic field, NMR probes the spin susceptibility via the hyperfine coupling (HFC) between the nuclear spin and the neighboring electronic spins. Since HFC is of short-range, it renders a nuclear site resolution, making it possible to differentiate the resonance of a nucleus in a local environment free of defect from the one situated in a defect-contaminated local environment. One common feature revealed by different NMR measurements is that the intrinsic spin susceptibility in these kagome compounds decreases rapidly at low temperatures, in striking contrast to the macroscopic susceptibility. With the persistent improvement of sample qualities, NMR is now possible to address the fundamental theoretical questions — “Is the ground state gapped or gapless?” and “What is the quantum number of the excitations?”.

---

* Corresponding author.
*E-mail address:* zheng-liu@tsinghua.edu.cn (Z. Liu).

https://doi.org/10.1016/j.scib.2019.08.028
2095-9273/

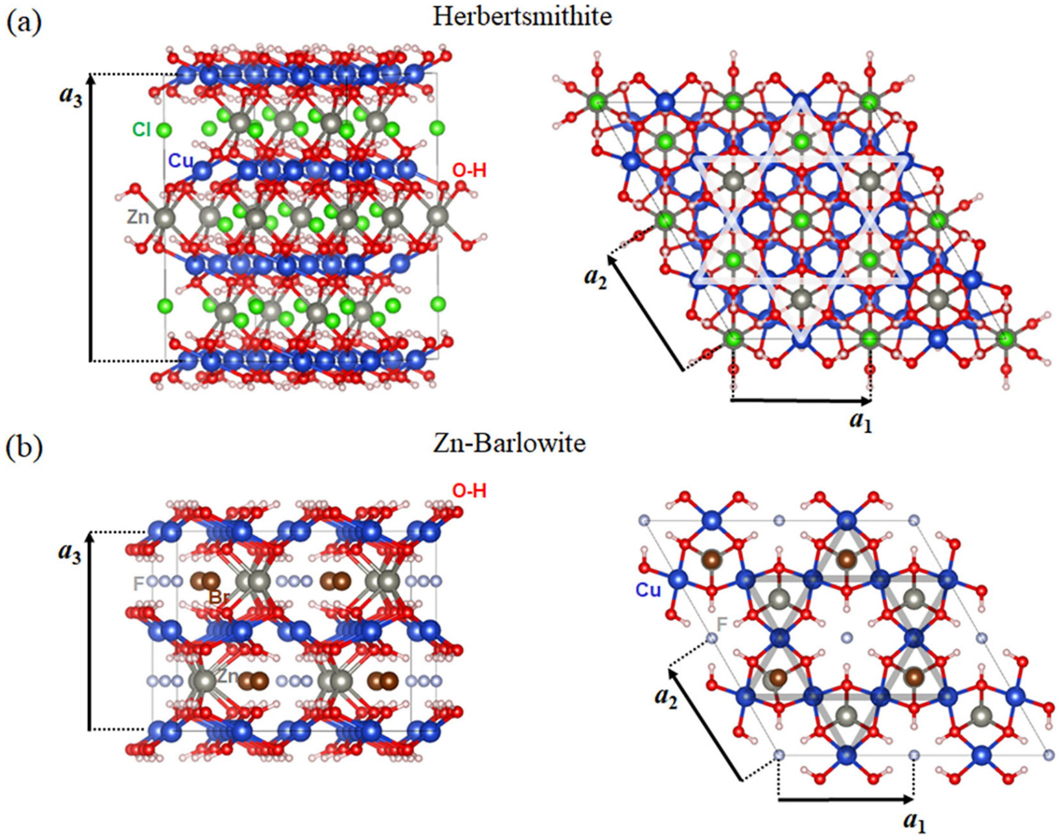

**Fig. 1.** (Color online) Crystal structures of (a) Herbertsmithite and (b) Zn-Barlowite. The kagome geometry of the $Cu^{2+}$ ions is indicated by shaded Stars of David in the top view. The three lattice vectors are marked by $a_{i=1,2,3}$.

Active investigations are underway to reach a consensus of opinion. One key issue is how to subtract the background defect signal accurately at low temperatures. Typically, the NMR peaks are convoluted by defect signals when the temperature goes down, making it tricky to naively identify the peak positions. It is worth noting that the smeared peaks in NMR spectra may come from random spin configurations, such as spin glass or valence bond glass as well [3].

The motivation of this article is to extend the application of the HFC calculation method as established for conventional magnetic systems [16–19] to QSL candidates. We note that since (spin) density functional theory (DFT) is practically a single-electron mean-field approach, it is traditionally perceived that hardly can any useful QSL information be inferred from this method. Interestingly, we realize that HFC represents an ideal property for DFT analysis without explicitly constructing the QSL wavefunction.

## 2. Basic aspects of NMR and HFC

A free nuclear spin in an external magnetic field ($B_{\text{ext}}$) exhibits a resonance frequency ($f_0$) due to the Zeeman effect. Embedded in a material, the nuclear resonance frequency will shift to $f$ due to the presence of internal magnetic field ($B_{\text{int}}$) induced by the electron spins. For example, Cl in Herbertsmithite, F in Zn-Barlowite and O in both compounds possess stable isotopes $^{35}$Cl, $^{19}$F and $^{17}$O with nuclear spin $I = 3/2$, 1/2, and 5/2, respectively, which have certain resonance frequencies. On the other hand, the electron spins in both compounds localize on the $Cu^{2+}$ ions, in the ideal case lying in the kagome planes (Fig. 1), which generates hyperfine field. We note that since QSL candidates are typically Mott (or charge-transfer) insulators, the chemical shift induced by orbital moment does not play an important role. In experiment, the chemical shift is commonly subtracted from the data as a temperature-independent constant.

The ratio between $B_{\text{int}}$ and the expectation value of the electron spin $\langle S \rangle$ is defined as the HFC constant, i.e.,

$$B^{I}_{\text{int}} = A^{I}_{\text{hf}} \langle S \rangle, \tag{1}$$

in which we add a label $I$ to denote different nuclear probes. We will focus on powder sample measurements, so the scalars in Eq. (1) are considered to be implicitly orientation averaged.

From the NMR shift, one can extract the information on the static electron spin susceptibility ($\chi_{\text{S}}$):

$$K^{I} \equiv \frac{f}{f_0} - 1 = \frac{B^{I}_{\text{int}}}{B_{\text{ext}}} = A^{I}_{\text{hf}} \chi_{\text{S}}(T). \tag{2}$$

Meanwhile, the static spin susceptibility can also be measured by macroscopic magnetometric methods, which we denote as $\chi^{\text{macro}}_{\text{S}}$. Whenever $K$ and $\chi^{\text{macro}}_{\text{S}}$ display a good linear correlation, a common practice to determine $A_{\text{hf}}$ experimentally is via the $K$-$\chi^{\text{macro}}_{\text{S}}$ slope.

Microscopically, $B_{\text{int}}$ has two origins [20,21]. A dipole field that captures the long-range anisotropic interaction:

$$(\mathbf{B}^{\text{dipole}}_{\text{int}})_{ij} = \frac{\mu_0 g_e \mu_B}{4\pi} \int \frac{\rho_s(\mathbf{r}+\mathbf{R}_I)}{r^3} \frac{3r_i r_j - \delta_{ij} r^2}{r^2} \mathrm{d}\mathbf{r}, \tag{3}$$

and the Fermi contact term that takes care of the non-vanishing unpaired electron wavefunction inside the nucleus:

$$B^{\text{Fermi}}_{\text{int}} = \frac{2\mu_0 g_e \mu_B}{3} \rho_s(\mathbf{R}_I), \tag{4}$$

in which $\mu_0$ is the vacuum permeability, $g_e$ is the electron $g$-factor, $\mu_B$ is the Bohr magnetic moment, $\rho_s$ is the electron spin density, and

$\mathbf{r}$ and $\mathbf{R}_I$ denote the coordination of electrons and nuclei, respectively.

For a powder sample, the crystal orientation is random and the external magnetic field is expected to have an equal probability to align with the three principle axes of $(\mathbf{B}_{\text{int}}^{\text{dipole}})_{ij}$. We thus evaluate $B_{\text{hf}}$ in Eq. (1) as the arithmetic average along the three principle directions:

$$B_{\text{int}}^{I} = B_{\text{int}}^{\text{Fermi}} + \text{Tr}[(\mathbf{B}_{\text{int}}^{\text{dipole}})_{ij}]/3 = B_{\text{int}}^{\text{Fermi}}. \quad (5)$$

Note that the matrix $(\mathbf{B}_{\text{int}}^{\text{dipole}})_{ij}$ is traceless. Under this approximation, the NMR peak frequency is dictated by the Fermi contact term, while the dipolar term contributes to peak broadening.

The key information to calculate $A_{\text{hf}}$ is nothing but $\rho_s(\mathbf{r})$. Note that $\langle S\rangle = \frac{1}{N}\int \rho_s(\mathbf{r})d\mathbf{r}$, where $N$ is a normalizing factor, depending on whether $\langle S\rangle$ is averaged to one unit cell or one magnetic atom etc. Therefore, two of the three quantities in Eq. (1) are directly calculable given $\rho_s(\mathbf{r})$, and $A_{\text{hf}}$ can be derived by taking the ratio.

## 3. DFT-based HFC calculation

### 3.1. Established methodology for conventional magnetic systems

Ground-state spin density is a calculable quantity exactly fit in DFT. Extensive efforts have been made to reliably reproduce $\rho_s$ in a variety of conventional magnetic systems, ranging from single atoms, clusters, metals and insulators [17–19,22,23]. An accurate representation of the core wavefunctions is the primary challenge. With the development of augmented basis functions, projector-augmented-waves pseudopotentials, as well as exchange–correlation functionals, the most widely used DFT codes can already achieve essential reproducibility [24,25], which presents a solid basis for our generalization to QSLs.

To compare with experiment, the previous calculations typically start with the experimental spin structures, and $\rho_s$ is determined iteratively by minimizing the DFT energy functional without including an external magnetic field. We should keep in mind that $\langle S\rangle$ in Eq. (1) is the expectation value of the electron spin under $B_{\text{ext}}$, instead of the ground-state expectation value. Therefore, such calculations only give the intrinsic hyperfine field, but ignore any $B_{\text{ext}}$-induced spin density change, e.g. polarization and canting. This issue is insignificant for a ferromagnet, in which $B_{\text{ext}}$ merely aligns the spins to a certain direction. For an antiferromagnet, however, one should only apply the calculation results to nuclear probes that predominantly experience the intrinsic hyperfine field, e.g. the probe is the magnetic ion itself. In contrast, when the nuclear probe resides in the middle of two antiferromagnetically coupled magnetic ions, the intrinsic hyperfine field largely cancels, whereas the HFC observed in experiment mainly arises from the ignored part.

### 3.2. Special considerations for QSL candidates

The aforementioned problem becomes even more severe for a QSL that by definition consists of fluctuating spins down to 0 K, i.e. without $B_{\text{ext}}$, $\langle S\rangle = 0$. It can be immediately seen that the intrinsic hyperfine field is exactly zero, and any measurable HFC arises from $B_{\text{ext}}$-induced polarization. A natural attempt is to first calculate the response of the QSL ground state to $B_{\text{ext}}$, and then do the HFC calculation based on that. However, this route is intimidating: not to mention how it can be described within DFT, it already costs tremendous efforts to calculate the susceptibility of QSL from simple effective models.

One interesting observation, as widely accepted in experiment, is that HFC in many cases is independent of temperature and magnetic field. If this perception is valid, it is possible to construct a practical calculation recipe without dealing with the exotic QSL wavefunction. Intuitively, when the temperature is comparable to the primary spin exchange, the system is actually far from the quantum regime, exhibiting the classical Curie-Weiss behavior. So imagine that at a moderate temperature, we hypothetically turn up $B_{\text{ext}}$. Then $\langle S\rangle$ will gradually increase (no matter how), and ultimately saturate. The real-space spin density of this fully-polarized state can be calculated directly using the established DFT method.

In short, we propose performing DFT-based HFC calculation on QSL candidates by choosing a fully-polarized reference state, and the derived HFC constant is expected to be directly comparable to experiment, so long as this constant is independent of $T$ and $B_{\text{ext}}$.

We note that there are known examples, in which the HFC constant varies with $T$ [26,27]. Therefore, in general one should examine first whether the application condition can be met. In the next subsection, we demonstrate that for Herbertsmithite and Zn-Barlowite the proposed calculation can be put on a firmer footing.

### 3.3. Formal justification for Herbertsmithite and Zn-Barlowite

In these two compounds, the electron spins arise from the $\text{Cu}^{2+}$ ions with a $3d^9$ valence configuration. Under the local Cu–O square crystal field, four of the five $3d$ orbitals are fully occupied, leaving a single electron at the $d_{x^2-y^2}$ orbital on top. We define the creation operator of this single electron as:

$$c_{i\sigma}^{\dagger} = \int d\mathbf{r} w(\mathbf{r}-\mathbf{R}_i) c_{\sigma}^{\dagger}(\mathbf{r}), \quad (6)$$

in which $i$ labels the Cu site and $\sigma = \uparrow, \downarrow$ labels the spin. Without loss of generality, the spin quantization direction is chosen to align with $B_{\text{ext}}$. The function $w(\mathbf{r}-\mathbf{R}_i)$ is the spatial wavefunction of this single electron, which predominantly consists of the $3d_{x^2-y^2}$ orbital. It is important to note that the function form of $w$ does not depend on $i$ and $\sigma$.

We can formally write the many-body eigenstates of this system as:

$$|\Phi_{\alpha}^{B}\rangle = f_{\alpha}^{B}(\{c_{i\sigma}^{\dagger}\})|0\rangle, \quad (7)$$

in which $\alpha$ labels the eigenstates with the corresponding eigenenergy $E_{\alpha}^{B}$. The label $B$ reminds that an external magnetic field is present that affects both the eigenstates and the eigenenergy. All the complexities of QSL are wrapped into the abstract function $f_{\alpha}^{B}(\{c_{i\sigma}^{\dagger}\})$, which in general takes the form of products and superposition of $\{c_{i\sigma}^{\dagger}\}$.

The expectation value of the electron spin $\langle S\rangle$ that appears in Eq. (1) can thus be calculated as:

$$\langle S\rangle = \frac{1}{Z}\sum_{\alpha} e^{-\beta E_{\alpha}} \langle\Phi_{\alpha}^{B}|c_{i\uparrow}^{\dagger}c_{i\uparrow} - c_{i\downarrow}^{\dagger}c_{i\downarrow}|\Phi_{\alpha}^{B}\rangle, \quad (8)$$

in which $Z = \sum_{\alpha} e^{-\beta E_{\alpha}}$ is the partition function. It is understood that in the absence $B_{\text{ext}}$, the correct QSL eigenstates $|\Phi_{\alpha}^{B=0}\rangle$ should give $\langle S\rangle = 0$. The equation demands that $|\Phi_{\alpha}^{B}\rangle$ maintains all the lattice symmetry. Therefore, all the $\text{Cu}^{2+}$ ions are equivalent, and $\langle S\rangle$ is independent of $i$.

The spin density $\rho_s$ that appears in Eqs. (3) and (4) can be calculated as:

$$\begin{aligned}\rho_s(\mathbf{r}) &= \frac{1}{Z}\sum_{\alpha} e^{-\beta E_{\alpha}} \langle\Phi_{\alpha}^{B}|c_{\uparrow}^{\dagger}(\mathbf{r})c_{\uparrow}(\mathbf{r}) - c_{\downarrow}^{\dagger}(\mathbf{r})c_{\downarrow}(\mathbf{r})|\Phi_{\alpha}^{B}\rangle \\ &= \sum_{i} |w(\mathbf{r}-\mathbf{R}_i)|^2 \langle S\rangle. \end{aligned} \quad (9)$$

The second equal sign is obtained by applying Eqs. (6) and (8). Combining Eqs. (1), (5) and (9), we have

$$A_{\rm hf}^{I} = \frac{2\mu_0 g_e \mu_B}{3} \frac{\rho_s(\mathbf{R}_I)}{\langle S\rangle} = \frac{2\mu_0 g_e \mu_B}{3} \sum_i |w(\mathbf{R}_I - \mathbf{R}_i)|^2. \tag{10}$$

Recall that $I$ denotes the chosen nuclear probe and $i$ denotes the Cu site. Eq. (10) indicates that $A_{\rm hf}$ only relies on the spatial distribution of the local electrons, while the complicated $f_\alpha^B(\{c_{i\sigma}^\dagger\})$ that dictates the many-body state are fully absorbed in $\langle S\rangle$ or equivalently $\chi_S$. When the local electrons are fully polarized, $\sum_i |w(\mathbf{R}_I - \mathbf{R}_i)|^2$ equals to the total spin density at $\mathbf{R}_I$, which rationalizes our calculation proposal.

It is worth reiterating that the justification above relies on (1) the orbital degree of freedom is frozen, and only spin is active to thermal fluctuation and the magnetic field; (2) $B_{\rm ext}$ does not induce spontaneous lattice symmetry breaking, and all the magnetic ions keep equivalent.

The last question is whether $\sum_i |w(\mathbf{R}_I - \mathbf{R}_i)|^2$ can be evaluated alternatively by explicitly constructing the local orbital $w$, e.g. via Wannierisation, based on a nonmagnetic calculation. In principle, yes, but the issue is that QSL candidates are typically Mott (or charge-transfer) insulators, and within a mean-field theory like DFT, the time-reversal symmetry has to be manually broken in order to open a charge gap. Without the gap opening, the hybridization between the local $d$-orbital and the anion $p$-orbitals are significantly overestimated [28]. Furthermore, for the purpose of HFC calculation, the precision of $w$ around the nuclear region is more important than its overall distribution. The former, typically a small quantity, may suffer from large errors during the orbital constructioin process. Therefore, it is most reliable and convenient to calculate the fully-polarized spin density based on the established HFC methodology (Table 1).

## 4. Computational details

We employ the HFC modules as implemented in WIEN2K [29] and VASP [30]. While both packages are based on DFT, the former is an all-electron (AE) scheme, which is expected to provide the most accurate description around the nucleus; the latter takes advantage of the pseudopotential (PP) approach to reduce the computation cost, but is still able to recover the full wavefunction near the nucleus via the projector-augmented-waves method [31,32].

The electron exchange-correlation functional parameterized by Perdew, Burke, and Ernzerhof (PBE) [33] is adopted. The strong correlation effect of the Cu-3$d$ orbitals is treated by the DFT + U method [34,35], which correctly reproduces the insulating charge gap of Herbertsmithite and Zn-Barlowite. We choose an effective interaction strength $U = 6$ eV following the previous works [28,36], which gives a gap size ~2 eV. $A_{\rm hf}$ does not sensitively depend on this choice, as long as $U$ is within a reasonable range. The dependence of the results on the $U_{\rm eff}$ value is summarized in Table 1.

For the PP-based calculations in VASP, we report the results calculated with an energy cutoff of 450 eV and a Γ-centered k-point grid. The grid density for unit cell is $8 \times 8 \times 6$, while for supercells only the Γ point is used. The convergence threshold for self-consistent-field calculations is $10^{-5}$ eV.

**Table 1**
Calculated $A_{\rm hf}^{\rm F}$, the magnetic moment of the $\rm Cu^{2+}$ ions, and the charge gap $\Delta$ in Zn-Barlowite $\rm Cu_3Zn(OH)_6FBr$, using different methods and $U_{\rm eff}$ values.

| Method | $U_{\rm eff}$ (eV) | $A_{\rm hf}^{\rm F}$ (kOe/$\mu_B$) | $M_{\rm Cu}$ ($\mu_B$) | $\Delta$ (eV) |
|---|---|---|---|---|
| AE | 4 | 2.522 | 0.732 | 1.40 |
| | 5 | 2.402 | 0.754 | 1.80 |
| | 6 | 2.284 | 0.776 | 2.22 |
| PP | 4 | 3.505 | 0.705 | 1.50 |
| | 5 | 3.300 | 0.727 | 1.79 |
| | 6 | 3.120 | 0.750 | 2.08 |

For the full potential augmented plane waves + local orbitals (APW + lo) calculations in WIEN2K, we set the radii of atomic spheres ($R_{\rm MT}$) 1.98, 2.14, 2.18, 2.50, 1.21 and 0.65 a.u. for Cu, Zn, F, Br, O, and H respectively. The plane-wave basis of the wave function in the interstitial region are truncated at $K_{\rm max} = 3.0/\min[R_{\rm MT}]$.

The lattice parameters are $a = b = 6.83$ Å, $c = 14.07$ Å for Herbertsmithite, and $a = b = 6.68$ Å, $c = 9.36$ Å for Zn-Barlowite, which are obtained from DFT + U relaxation with the fully-polarized spin configuration. These calculated lattice parameters are in good agreement with experimental values: $a = b = 6.8342$ Å, $c = 14.0320$ Å for Herbertsmithite [9], and $a = b = 6.66782$ Å, $c = 9.3079$ Å for Zn-Barlowite [13]. Atomic positions are also optimized until the forces are smaller than 0.01 eV/Å. For the defect structures, the HFC constants are obtained by simply making the chemical substitution, with fixed lattices and atomic positions. A systematic study on defect-induced structural distortion and symmetry breaking is beyond the scope of the current calculation. Some simple tests show that the distortion will modify the short-range HFC values quantitatively.

## 5. Benchmark tests

We apply the proposed calculation method to evaluate $A_{\rm hf}$ of Cl in Herbertsmithite, F in Zn-Barlowite and O in both compounds. Except for O in Zn-Barlowite, experimental $A_{\rm hf}$ values fitted from the $K$-$\chi_S^{\rm marco}$ slope have been reported. We note that the coefficients in Eqs. (3) and (4) are derived in SI units, and the unit of $A_{\rm hf}$ is Tesla (T). On the other hand, the commonly-used HFC unit in experiment is kOe/$\mu_B$. The conversion is made by normalizing the total spin density such that the magnetic moment of each $\rm Cu^{2+}$ is 1 $\mu_B$, and by multiplying a factor of 10 to convert T into kOe.

A comparison is made in Fig. 2a. The overall agreement between the calculation and the experiment [10,11,13] is very good. Not only the magnitude variation but also the sign of $A_{\rm hf}$ is correctly reproduced by our calculation. In both compounds, $A_{\rm hf}$ at the O site is at least one order of magnitude larger than that at the halogen site because of the shorter Cu-O distance. In Herbertsmithite, $A_{\rm hf}$ at the Cl site is negative, indicating that the nuclear feels a $B_{\rm int}$ opposite to $B_{\rm ext}$, and thus the larger $\chi_s$ is, the lower the frequency will $K_s$ shift to. We should point out that when $A_{\rm hf}$ is small, e.g. for the Cl and F cases, the spin density tail at the nuclear site becomes extremely low, so one has to expect a relatively larger error using the experimental value $A_{\rm hf}^{\rm exp}$ as a measure. It appears that the AE method can always reduce the error slightly compared with the PP method, but generally the latter has an adequate accuracy. The inevitable presence of defects in real samples should also have contributed to the differences between the experimental and calculated $A_{\rm hf}$.

## 6. Analysis of defect effects

With the benchmark calculation on pristine unit cells, we now proceed to apply this method to defect structures. Considering that the defect simulation is computational demanding, we rely on the less costly pseudopotential method. Three typical types of Cu-Zn defects are created in a large supercell structure: (a) substituting an inter-kagome Zn with Cu ($\rm Cu_{Zn}$), which leads to an extra spin site; (b) substituting a kagome Cu with Zn ($\rm Zn_{Cu}$), which results in a spin vacancy; and (c) a $\rm Cu_{Zn}$+$\rm Zn_{Cu}$ antisite pair. We note that in the present work, the relaxation of the lattice structure around the defects is not taken into account. It is understood that

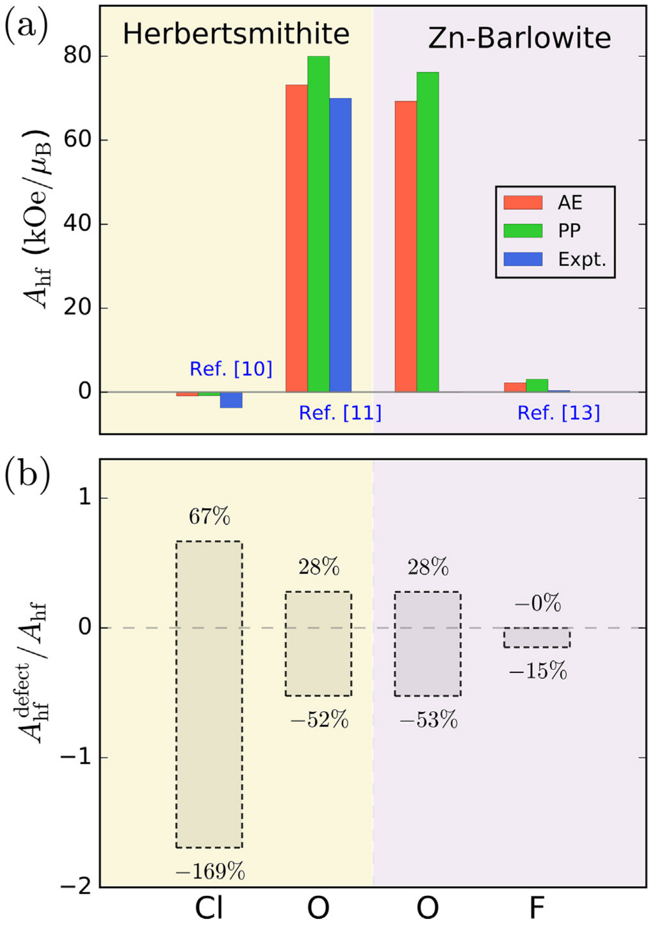

**Fig. 2.** (Color online) (a) Calculated HFC constants of Cl and O in Herbertsmithite, and O and F in Zn-Barlowite, with available NMR experimental data for comparison. "AE" and "PP" represent all-electron and pseudopotential calculation results respectively. (b) Calculated variation range of HFC when Cu-Zn defects are present. The definition of $A_{\rm hf}^{\rm defect}$ is given in Eq. (11).

structural distortion will also affect the HFC constant. We will leave this effect for future investigation.

### 6.1. HFC variation

Fig. 3a and b show $A_{\rm hf}$ in Herbertsmithite as a function of the distance ($d$) between the defect and the selected nuclear sites (O and Cl). Fig. 3c and d display the defect structures and highlight the strongly perturbed nuclei. These results reveal remarkable differences between O and Cl: it is clear from Fig. 3a that $A_{\rm hf}^{\rm O}(d)$ falls sharply back to the defect-free level beyond 2 Å. In contrast, $A_{\rm hf}^{\rm Cl}(d)$ has a long tail (Fig. 3b). At the O site closest to the defect, an extra spin ($\rm Cu_{Zn}$) results in a larger $\rho_s(\mathbf{R}_I)$ in Eq. (4), and thus $A_{\rm hf}^{\rm O}$ increases; a spin vacancy ($\rm Zn_{Cu}$) cuts $A_{\rm hf}^{\rm O}$ nearly by half; an antisite pair acts in both ways, depending on the O location. These features are intuitive within a classical picture. In contrast, $\rm Cu_{Zn}$ reduces $A_{\rm hf}^{\rm Cl}$, suggesting that instead of contributing additive spin density, this inter-kagome spin draws spin density away from Cl. In addition, the $\rm Zn_{Cu}$-induced change of $A_{\rm hf}^{\rm Cl}$ exhibits an oscillation with distance, e.g. at the NN site $A_{\rm hf}^{\rm Cl}$ increases, while at the next NN site $A_{\rm hf}^{\rm Cl}$ decreases. An antisite pair gives rather complicated distribution of $A_{\rm hf}^{\rm Cl}$ (Fig. 3d).

Fig. 4 shows the results of Zn-Barlowite. The behavior of O is very similar to that in Herbertsmithite. Interestingly, F is quite different from Cl. It is clear that F is also a nearsighted probe, and all the simulated defects reduce $A_{\rm hf}$ at the NN F site.

We can define the change of $A_{\rm hf}(d)$ from the defect-free level as a measure of the defect-induced HFC:

$$A_{\rm hf}^{\rm defect}(d) = A_{\rm hf}(d) - A_{\rm hf}(d \to \infty),$$

where $A_{\rm hf}(d \to \infty)$ converges to the $A_{\rm hf}$ values calculated in a pristine unit cell. Fig. 2b summarizes the distribution of $A_{\rm hf}^{\rm defect}(d)$ with respect to the four nuclear probes. Cl suffers from the largest relative variation, O in between, and F is least affected by the defects.

Our numerical simulation confirms that O is an excellent probe of the intrinsic kagome physics - the intrinsic $A_{\rm hf}$ is large and the nearsightedness ensures that only a small fraction of O sites is located in an effective magnetic field contaminated by the defects. In contrast, the nonlocal and oscillating $A_{\rm hf}^{\rm defect}$ of Cl in Herbertsmithite inevitably hinders a transparent extraction of $\chi_S^{\rm kagome}(T)$ from the NMR shift. F in Zn-Barlowite also represents a good local probe. Despite a small coupling to the kagome Cu, F is at the same time less affected by the defects. Its $A_{\rm hf}^{\rm defect}/A_{\rm hf}$ ratio is even smaller than that for O (Fig. 2b).

We would like to mention that the recent $^{17}$O NMR measurement on single-crystal Herbertsmithite [37] clearly resolved two sets of resonance peaks, one from the O sites in defect-free environment and the other from the O sites closest to the defects. The latter roughly experiences a $A_{\rm hf}$ half of the strength of the former, in agreement with the calculated lower bound of $A_{hf}^{\rm defect}$ as shown in Fig. 2b. In our calculation, this half $A_{\rm hf}$ corresponds to the NN O sites around a $\rm Zn_{Cu}$ defect, which has an intuitive explanation as one of the two neighboring Cu ions is missing. This scenario was also presumed in an earlier powder $^{17}$O NMR measurement [11], but the new single-crystal experiment [37] showed evidence that this half $A_{\rm hf}$ should be assigned to the NN O sites around a $\rm Cu_{Zn}$ defect. The exact type of defects in the samples remains an important question requiring further investigations.

### 6.2. Experimental implications

It is understood that the existence of defects perturbs both $A_{\rm hf}$ and $\chi_S$ in Eq. (2). $\rm Cu_{Zn}$ represents the simplest case, which can be considered as a nearly free spin [10], and the NMR shift of a probe nucleus affected by this defect has the form:

$$\begin{aligned} K(d) &= A_{\rm hf}\chi_S^{\rm kagome}(T) + A_{\rm hf}^{\rm defect}(d)\chi_S^{\rm defect}(T) \\ &= A_{\rm hf}\chi_S^{\rm kagome}(T) + \frac{A_{\rm hf}^{\rm defect}(d)C}{T}, \end{aligned} \tag{12}$$

where $C$ is the Curie constant. The intrinsic NMR shift $A_{\rm hf}\chi_S^{\rm kagome}(T)$ is thus split into a spectrum of satellite peaks due to the additional defect term. The number of satellite peaks is dictated by the distribution of $A_{\rm hf}^{\rm defect}(d)$, and the peak height is proportional to the population of the specific nuclear sites. Depending on the sign of $A_{\rm hf}^{\rm defect}(d)$, the satellite peaks can undergo either a blueshift or a redshift. The shift grows rapidly as $T \to 0$, because of the Curie behavior of the defect susceptibility. When the frequency resolution is low, these satellite peaks simply merge into a broad envelope, and the defect term is responsible for a temperature-dependent envelope width. In powder samples, the half-height-full-width of the broad NMR envelop indeed displays a Curie behavior [10], just like $\chi_S^{\rm macro}$.

It is insightful to consider one concrete example by plugging in Eq. (12) the calculated $A_{\rm hf}^{\rm defect}$ values. We select F in Zn-Barlowite (Fig. 5), for which a direct comparison can be made against the experimental Fig. 3a in Ref. [13]. We adopt the same fitting formula of $\chi_S^{\rm kagome}(T)$ as used in the experimental paper [13]. For each

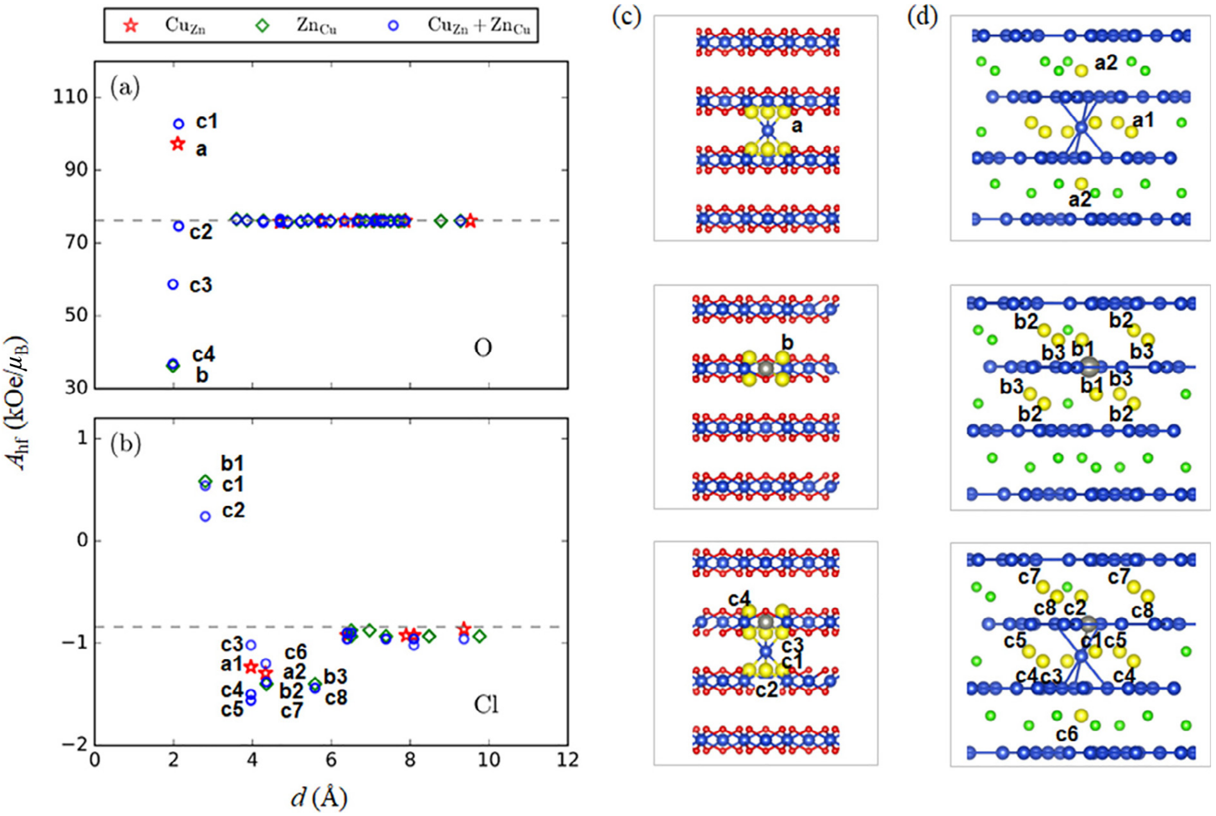

**Fig. 3.** (Color online) Calculated $A_{hf}$ of (a) O and (b) Cl in Herbertsmithite in the presence of three types of Cu-Zn defects. The $A_{hf}$ values vary as a function of distance between the probe nuclei and the defect. For the $Cu_{Zn} + Zn_{Cu}$ pair, the distance is measured depending on which defect atom is closer. The horizontal dash lines indicate the $A_{hf}$ values calculated in the pristine crystal. The strongly perturbed nuclei are marked by letters and numbers, with their positions highlighted in (c) and (d). For clarity, only Cu and the probe nuclei are shown.

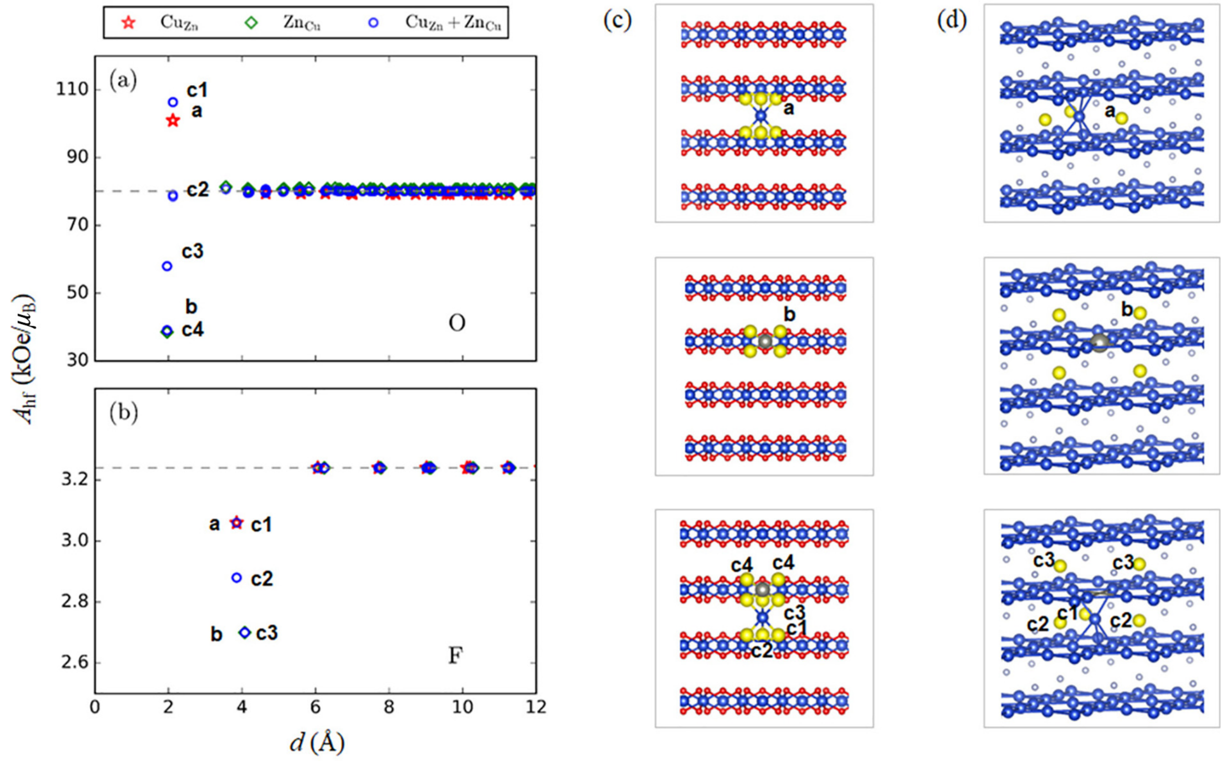

**Fig. 4.** (Color online) Calculated $A_{hf}$ of (a, c) O and (b, d) F in Zn-Barlowite in the presence of three types of Cu-Zn defects. The meaning of the labels is the same as in Fig. 3.

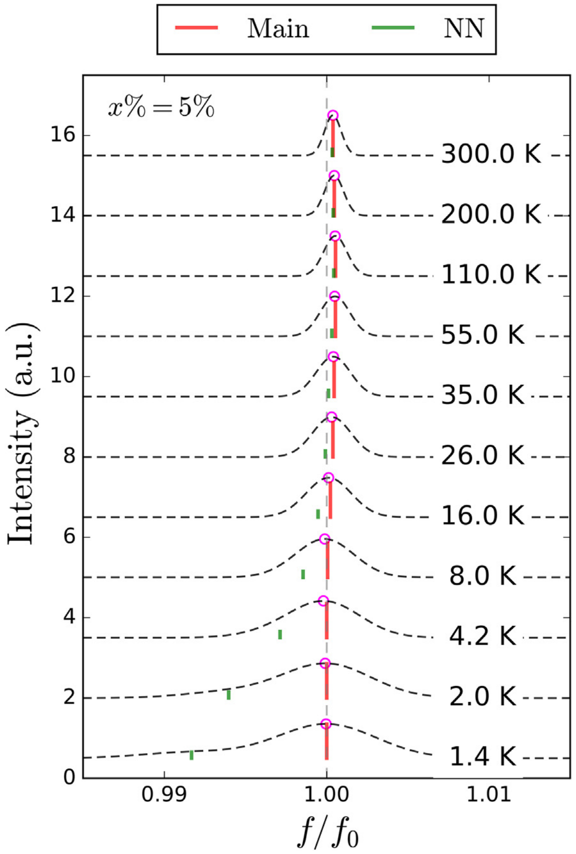

**Fig. 5.** (Color online) Simulated $^{19}$F NMR spectra in Zn-Barlowite with 5% $Cu_{Zn}$ defects at varying temperature. The red and green bars represent the resonance peak of nuclei far away and nearest to the defect, respectively. The dashed curve serves as a guide for eyes, reflecting that when the defect types become more complex, more satellite peaks exist in between, and merge into a smooth envelop.

experimental temperature, we calculate the NMR shift at the F sites far from a defect and the F sites nearest to a $Cu_{Zn}$, and mark in Fig. 5 with two bars. The bar height is proportional to the population of the corresponding sites. We assume that when the defect type becomes more complex, the other types of F sites in general experience a HFC strength in between these two bars, which merge together into a smooth peak. We can see that the broadening of the NMR peak as temperature drops as observed in the experiment can be naturally explained. Another feature is that the merged envelope has a higher shoulder on the low-frequency side, which arises from the negative sign of $A_{hf}^{defect}$ at the F site.

## 7. Perspectives

In collaboration with the NMR experimentalists, we expect that the input of $A_{hf}^{defect}$ will help formulate a more effective way to separate out the defect signals in the low-$T$ data, pinning down the nature of the long-sought QSL state.

From the computational side, the calculation method proposed here still requires further examination of its general applicability, by applying to a wider range of QSL candidates. One open question is when the spins in a system have drastically different local susceptibility whether a fully-polarized reference state still works. It also remains to be determined when the spin density around a nuclear site is extremely low, generally how accurate the numerical results will be.

Traditionally, quite different from the discovery of other exotic quantum materials, such as topological insulators and semimetals, first-principles method was less involved in the search of QSLs, because rarely their properties could be reliably calculated within the DFT framework. We expect that the HFC predictive potential will stimulate broader interests from the DFT community in this rapidly growing field [38], which in turn may shed some new light into understanding the defect-masked QSL physics.

## Conflict of interest

The authors declare that they have no conflict of interest.

## Acknowledgments

We would like to acknowledge J.-W. Mei, Z. Li and G.Q. Zheng for stimulating this work. This work was supported by the National Natural Science Foundation of China (11774196) and Tsinghua University Initiative Scientific Research Program. S.Z. is supported by the National Postdoctoral Program for Innovative Talents of China (BX201600091) and the Funding from China Postdoctoral Science Foundation (2017M610858). F.L. acknowledges the support from US-DOE (DEFG02-04ER46148). Y.Z. is supported by National Key Research and Development Program of China (2016YFA0300202), National Natural Science Foundation of China (11774306), and the Strategic Priority Research Program of Chinese Academy of Sciences (XDB28000000).

## Author contributions

Zheng Liu conceived the idea and designed the project. Shunhong Zhang performed the calculations. All authors analyzed the results and wrote the manuscript.

## References

[1] Balents L. Spin liquids in frustrated magnets. Nature 2010;464:199.
[2] Savary L, Balents L. Quantum spin liquids: a review. Rep Prog Phys 2017;80:016502.
[3] Zhou Y, Kanoda K, Ng T-K. Quantum spin liquid states. Rev Mod Phys 2017;89:025003.
[4] Wen XG. Mean-field theory of spin-liquid states with finite energy gap and topological orders. Phys Rev B 1991;44:2664–72.
[5] Anderson PW. The resonating valence bond state in $La_2CuO_4$ and superconductivity. Science 1987;235:1196–8.
[6] Lee PA, Nagaosa N, Wen X-G. Doping a mott insulator: physics of high-temperature superconductivity. Rev Mod Phys 2006;78:17–85.
[7] Norman MR. Colloquium Herbertsmithite and the search for the quantum spin liquid. Rev Mod Phys 2016;88:041002.
[8] Lee PA. An end to the drought of quantum spin liquids. Science 2008;321:1306–7.
[9] Shores MP, Nytko EA, Bartlett BM, et al. A structurally perfect $S = 1/2$ kagome antiferromagnet. J Am Chem Soc 2005;127:13462–3.
[10] Imai T, Nytko EA, Bartlett BM, et al. $^{63}$Cu, $^{35}$Cl, and $^{1}$H NMR in the $S = 1/2$ kagome lattice $ZnCu_3(OH)_6Cl_2$. Phys Rev Lett 2008;100:077203.
[11] Olariu A, Mendels P, Bert F, et al. $^{17}$O NMR study of the intrinsic magnetic susceptibility and spin dynamics of the quantum kagome antiferromagnet $ZnCu_3(OH)_6Cl_2$. Phys Rev Lett 2008;100:087202.
[12] Liu Z, Zou X, Mei J-W, et al. Selectively doping barlowite for quantum spin liquid: a first-principles study. Phys Rev B 2015;92:220102.
[13] Feng Z, Li Z, Meng X, et al. Gapped spin-1/2 spinon excitations in a new kagome quantum spin liquid compound $Cu_3Zn(OH)_6FBr$. Chin Phys Lett 2017;34:077502.
[14] Pasco CM, Trump BA, Tran TT, et al. Single-crystal growth of $Cu_4(OH)_6BrF$ and universal behavior in quantum spin liquid candidates synthetic barlowite and herbertsmithite. Phys Rev Mater 2018;2:044406.
[15] Mendels P, Bert F. Quantum kagome frustrated antiferromagnets: one route to quantum spin liquids. Comp Rend Phys 2016;17:455–70.
[16] Jena P, Mahanti SD, Das TP. Theory of isotropic and anisotropic knight shift in beryllium. Phys Rev Lett 1968;20. 977–977.
[17] Declerck R, Pauwels E, Van Speybroeck V, et al. First-principles calculations of hyperfine parameters with the gaussian and augmented-plane-wave method: application to radicals embedded in a crystalline environment. Phys Rev B 2006;74:245103.
[18] Bahramy MS, Sluiter MHF, Kawazoe Y. First-principles calculations of hyperfine parameters with the all-electron mixed-basis method. Phys Rev B 2006;73:045111.

[19] Kadantsev ES, Ziegler T. First-principles calculation of parameters of electron paramagnetic resonance spectroscopy in solids. Magn Reson Chem 2010;48: S2–S10.
[20] Slichter CP. Principles of magnetic resonance, With Examples from Solid State Physics. Springer; 1990.
[21] Blügel S, Akai H, Zeller R, et al. Hyperfine fields of 3d and 4d impurities in nickel. Phys Rev B 1987;35:3271–83.
[22] Carlier D, Ménétrier M, Grey CP, et al. Understanding the NMR shifts in paramagnetic transition metal oxides using density functional theory calculations. Phys Rev B 2003;67:174103.
[23] Partzsch S, Wilkins SB, Hill JP, et al. Observation of electronic ferroelectric polarization in multiferroic $YMn_2O_5$. Phys Rev Lett 2011;107:057201.
[24] Novák P, Kune J, Pickett WE, et al. Self-interaction correction and contact hyperfine field. Phys Rev B 2003;67:140403.
[25] Novák P, Chlan V. Contact hyperfine field at Fe nuclei from density functional calculations. Phys Rev B 2010;81:174412.
[26] Kitagawa K, Katayama N, Ohgushi K, et al. Commensurate itinerant antiferromagnetism in $BaFe_2As_2$: $^{75}$As-NMR studies on a self-flux grown single crystal. J Phys Soc Jpn 2008;77:114709.
[27] Li J, Lei B, Zhao D, et al. A spin-orbital-intertwined nematic state in FeSe. arXiv:1903.05798, 2019.
[28] Liu Z, Mei J-W, Liu F. First-principles study of the organometallic $S = 1/2$ kagome compound Cu(1,3-bdc). Phys Rev B 2015;92:165101.
[29] Blaha P, Schwarz K, Madsen GKH, et al. WIEN2K, an augmented plane wave + local orbitals program for calculating crystal properties, Karlheinz Schwarz. Austria: Techn. Universität Wien; 2001.
[30] Kresse G, Furthmüller J. Efficient iterative schemes for ab initio total-energy calculations using a plane-wave basis set. Phys Rev B 1996;54:11169–86.
[31] Blöchl PE. Projector augmented-wave method. Phys Rev B 1994;50:17953–79.
[32] Kresse G, Joubert D. From ultrasoft pseudopotentials to the projector augmented-wave method. Phys Rev B 1999;59:1758–75.
[33] Perdew JP, Burke K, Ernzerhof M. Generalized gradient approximation made simple. Phys Rev Lett 1996;77:3865–8.
[34] Anisimov VI, Solovyev IV, Korotin MA, et al. Density-functional theory and NiO photoemission spectra. Phys Rev B 1993;48:16929–34.
[35] Dudarev SL, Botton GA, Savrasov SY, et al. Electron-energy-loss spectra and the structural stability of nickel oxide: an LSDA+U study. Phys Rev B 1998;57:1505–9.
[36] Jeschke HO, Salvat-Pujol F, Valentí R. First-principles determination of Heisenberg Hamiltonian parameters for the spin-$\frac{1}{2}$ kagome antiferromagnet $ZnCu_3(OH)_6Cl_2$. Phys Rev B 2013;88:075106.
[37] Fu M, Imai T, Han T-H, et al. Evidence for a gapped spin-liquid ground state in a kagome Heisenberg antiferromagnet. Science 2015;350:655–8.
[38] Nikolaev SA, Solovyev IV, Ignatenko AN, et al. Realization of the anisotropic compass model on the diamond lattice of $Cu^{2+}$ in $CuAl_2O_4$. Phys Rev B 2018;98:201106.

Shunhong Zhang received his Ph.D. degree in 2016 from Peking University and worked as a postdoc at Institute for Advanced Study, Tsinghua University during 2016–2018. He joined University of Science and Technology of China in 2018. He is interested in several topics of computational materials science and condensed matter physics, including magnetic materials, topological materials, and superconductors.

Zheng Liu obtained his Ph.D. degree at Institute for Advanced Study, Tsinghua University in 2012, and is currently an Associate Member at the same institute. His research interest lies in the intersection of condensed matter physics and materials science, particularly focusing on bridging the frontier of condensed matter theory, such as topological order, fractionalization and quantum frustration, with real-world materials.